Journal of The Electrochemical Society, **158** (3) A309-A315 (2011)
0013-4651/2011/158(3)/A309/7/$28.00 © The Electrochemical Society

Synthesis and Electrochemical Properties of Monoclinic $LiMnBO_3$ as a Li Intercalation Material

Jae Chul Kim,[z] Charles J. Moore,[*,z] Byoungwoo Kang,[z] Geoffroy Hautier,[z] Anubhav Jain,[*,z] and Gerbrand Ceder[,z]**

Department of Materials Science and Engineering, Massachusetts Institute of Technology, Cambridge, Massachusetts 02139, USA

We investigated the structural stability and electrochemical properties of $LiMnBO_3$ in the hexagonal and monoclinic form with ab initio computations and, for the first time, report electrochemical data on monoclinic $LiMnBO_3$. In contrast to the negligible Li-storage capacity in the hexagonal $LiMnBO_3$, a second cycle discharge capacity of 100 mAh/g was achieved in the monoclinic $LiMnBO_3$, with good capacity retention over multiple cycles. Elevated temperature cycling indicates that the capacity of monoclinic $LiMnBO_3$ is kinetically limited, and further improvement may be expected by addressing the Li ion and/or electron transport limitations.
 [DOI: 10.1149/1.3536532]

Manuscript submitted October 13, 2010; revised manuscript received December 17, 2010. Published January 20, 2011.

Rechargeable lithium batteries use intercalation oxides as cathodes as they can reversibly store large amounts of Li^+ ions and electrons. While most cathodes used in commercial cells are layered oxides, materials containing polyanion groups such as phosphate (PO_4), silicate (SiO_4), and borate (BO_3) have generated interest because of the inherent stability of the polyanion group against oxygen loss.[1-4] Among them, $LiFePO_4$ is currently considered a successful polyanionic intercalation cathode due to its potential for low cost, high stability, low toxicity, and high rate capability, as well as long cycle life.[4-7]

The development of new cathode materials with high capacity, good stability, and high safety is important for the future improvement of Li batteries. In our search for new cathode materials, we have focused on borates as they contain the lightest and stable polyanion group. By using ab initio computations, we have searched through a large number of possible borates for materials that may show a good electrochemical performance as a Li-intercalation cathode. Ab initio computations can nowadays predict with a reasonable accuracy essential battery properties such as voltage, stability, and safety.[8-10] Our search used voltage, theoretical capacity, stability as measured by the driving force for phase transformation of the charged and discharged state, and safety as measured by the oxidation strength of the charged cathode as screening criteria.[9-13] This large-scale and unbiased screening identified both hexagonal and monoclinic $LiMnBO_3$ as potential high energy density lithium ion battery cathode materials. Hexagonal $LiMnBO_3$ with a theoretical capacity of 222 mAh/g has already been studied in the literature but has thus far displayed a very low electrochemical activity with a negligible capacity of 6 mAh/g even at a very slow charging and discharging rate.[3,14] One recent report on hexagonal $LiMnBO_3$ claims an initial discharge capacity of 75.5 mAh/g but with a very wide voltage window range, 4.8–1.0 V, making it likely that the capacity reflects a conversion reaction rather than intercalation.[15]

In this paper, we focus on the monoclinic polymorph of $LiMnBO_3$, with C12/c1 symmetry.[16] Even though this polymorph has been previously studied, no electrochemical data have been reported on it.[16,17] Therefore, in this work, monoclinic $LiMnBO_3$ was synthesized and electrochemically evaluated in order to investigate its possibility as a cathode material for lithium ion batteries.

Computational Methodology and Experimental Procedures

Computation.— Ab initio computations on the hexagonal and monoclinic $LiMnBO_3$ polymorphs were performed with the density functional theory (DFT) framework using the generalized gradient approximation with Hubbard U corrections (GGA + U).[18,19] The GGA + U approach has been well tested to predict voltages and phase stability.[10,20,21] A value of 3.9 is used for the *d* states on Mn, as determined by fitting experimental oxidation energies via the method of Wang et al.[22] All calculations were performed with the Vienna Ab initio Simulation Package (VASP) with the supplied projector-augmented pseudopotentials.[23,24]

Total energies were computed for all the structures in the Inorganic Crystal Structure Database (ICSD) phases containing Li, Mn, B, and O.[25] The $LiMnBO_3$ monoclinic phase is referenced in the ICSD with partial occupancies on Li and Mn sites (ICSD number: 200535).[16] An ordered version of this structure was generated from this entry using an enumeration technique as presented in Hart and Forcade[26] and picking the Li/Mn distribution with the lowest electrostatic energy. Table I presents this ordered $LiMnBO_3$ monoclinic structure. To evaluate the stability of $LiMnBO_3$ and $MnBO_3$ phases against decomposition (i.e., "distance to hull"), we computed 0 K phase diagrams according to the methodology outlined by Ong et al.[12]

To determine the intermediate Li-vacancy configurations along the $LiMnBO_3$–$MnBO_3$ line, we tested several different lithium orderings for supercells up to 75 atoms in size. We calculated DFT energies for 20 symmetrically distinct Li orderings for each intermediate composition and chose the lowest energy ordering as the ground state. The 20 orderings were chosen by first enumerating all possible Li orderings and then determining the structures lowest in electrostatic energy as determined by Ewald summation.[26,27]

Barriers for Li diffusion were calculated for the fully lithiated and fully delithiated limits using the nudged elastic band method.[28] The diffusion pathways calculated correspond to one-dimensional (1D) Li diffusion via hops between nearest neighbor Li sites. To avoid problems with charge ordering, plain GGA (as opposed to GGA + U) was used for the elastic band calculations. Calculations were performed on supercells containing either a single Li vacancy or a single Li atom for the lithiated and delithiated states, respectively. The lattice parameters were fixed at the optimized GGA + U lattice parameters of the nondefected structure. The supercell size was $1 \times 1 \times 3$ for the hexagonal cells and $2 \times 2 \times 1$ for the monoclinic cells.

Synthesis.— $LiMnBO_3$ samples were synthesized by mixing stoichiometric amounts of Li_2CO_3, $MnC_2O_4 \cdot 2H_2O$, and H_3BO_3. The raw powders were dispersed into acetone, ballmilled for 72 h, and then dried. The mixture was fired at 350°C for 10 h under an argon atmosphere. After careful grinding by mortar and pestle, the specimens were pressed into a disk-shaped pellet and sintered at 500–800°C for 10 h under an argon atmosphere. Some samples were also prepared with carbon coating. In order to coat a conduc-

* Electrochemical Society Student Member.
** Electrochemical Society Active Member.
[z] E-mail: jaeck@mit.edu; c_moore@mit.edu; bwkang@mit.edu; hautierg@mit.edu; anubhavj@mit.edu; gceder@mit.edu

Table I. Computed properties of the $LiMnBO_3$ polymorphs.

Phase	Average Voltage (V)	Theoretical Grav. Energy Density (Wh/kg)	Theoretical Vol. Energy Density (Wh/L)	Theoretical Capacity (mAh/g)	Lithiated Distance to Hull[a] (meV/at.)	Delith. Distance to Hull[a] (meV/at.)	Volume Change[b] (%)
Hexagonal	4.11	912	2922	222	0	216	0.6
Monoclinic	3.70	822	2635	222	4	140	2.5

[a] Distance to hull stands for difference in energy from the computed ground state.
[b] Volume change is taken as a percentage of the lithiated state volume.

tive carbon phase on the particle surface, the pellet was manually ground, and 10 wt % of sucrose was mixed with the ground sintered powder by planetary ballmilling for 12 h. The specimen was then annealed at 500°C for 5 h under an argon atmosphere.

Structure and morphology analysis.— In order to analyze the crystal structure, the particle size, particle morphology, X-ray diffraction (XRD), scanning electron microscopy (SEM), and transmission electron microscopy (TEM) were performed, respectively. The X-ray patterns were obtained on a Rigaku Diffractometer using Cu Kα radiation by step scanning in the 2θ range of 10–80°. Rietveld refinement and profile matching of the powder diffraction data were performed with X'pert HighScorePlus using space group C12/c1 and P-6 for $LiMnBO_3$. SEM images were collected on a FEI Philips XL30 field-emission gun (FEG) environmental scanning electron microscopy (ESEM). The SEM samples were coated with palladium to prevent charging. A high resolution transmission electron microscopy (HRTEM) image was obtained under an accelerating voltage of 200 keV on a JEOL 2010 FEG analytical electron microscope. The specimen was suspended on a copper grid with lacey carbon.

Electrochemistry.— The cathode was composed of 80 wt % active material, 15 wt % carbon black, and 5 wt % polytetrafluoroethylene (PTFE). These components were manually mixed inside an argon-filled glove box. In some cases, the appropriate amount of the active material and carbon black were mixed with planetary ballmilling for 30 min to blend $LiMnBO_3$ with carbon better, and then PTFE was added and mixed manually. The amount of C-coating was identified by combustion infrared detection (ASTM E 1019-08), and the actual amount of $LiMnBO_3$ in the electrode was 77 wt % when carbon coated. The specific capacities of C-coated $LiMnBO_3$ were calculated based on these data; 1 M of $LiPF_6$ in 1:1 ratio of ethylene carbonate:dimethyl carbonate (EC:DMC) solution, Celgard 2500, and Li metal foil were used as an electrolyte, the separators, and the counter electrode, respectively. The coin cells or Swagelok cells were assembled inside an argon-filled glove box and tested on a Maccor 2200 at room temperature. Electrochemical tests were also performed at an elevated temperature (60°C). The loading density of the cathode was approximately 3 mg/cm^2. The current density at 1 C was based on the theoretical capacity of 222 mAh/g. All cell tests had 1 min open-circuit rest at the end of each charge and discharge.

Results and Discussion

Results.— The crystal structures of the $LiMnBO_3$ polymorphs are shown in Fig. 1. The reported hexagonal structure consists of columns of edge-sharing square pyramidal Mn sites joined by planar borate and tetrahedral lithium sites.[3] The monoclinic structure is reported with a small amount of disorder, whereby each trigonal-bipyramidal Li and Mn site is split into both an upper site and a lower site.[16] Due to the close proximity of these sites, this splitting has been interpreted as follows: while any given lithium or manganese ion may sit in either the upper or lower portion of the bipyramid, both may not be occupied simultaneously. In turn, this implies that each trigonal-bipyramid will be occupied by a single ion at all times. Electrostatic calculations predicted, and ab initio calculations confirm, that the most stable ordering is when all Li and Mn ions sit on the same side of the bipyramids, as shown in Fig. 1 by the green and blue spheres.

By using ab initio computations, we evaluated the lithium redox voltage and energy density with respect to a Li anode, volume change, and thermodynamic stability in the charged and discharged state for both the monoclinic and hexagonal $LiMnBO_3$ (Table I). The computationally identified ground state for $MnBO_3$ is a stoichiometric mixture of Mn_2O_3, MnO_2, and MnB_4O_7. The computationally predicted ground state for $LiMnBO_3$ is the hexagonal phase, although its energy difference with the monoclinic phase of 5 meV per atom is close to the limit of numerical accuracy for our methods and is small enough to be easily overcome by entropic effects. Figure 2 shows the calculated formation energies of monoclinic $LiMnBO_3$ as a function of the Li content and the corresponding voltage profile. The average computed average redox voltage over the full capacity range is approximately 3.70 V, whereas the computed voltage in the capacity range currently accessible by experiments is approximately 3.4 V.

Figures 3a and 3b show the schematic diagrams of the calculated Li diffusion pathways in the hexagonal and monoclinic $LiMnBO_3$ unit cell, respectively. To highlight the diffusion pathway, an isoenergy surface for Li position is plotted. This isoenergy surface is obtained from an empirical energy model consisting of screened electrostatics and a repulsive Li–O pair potential. Even though we use an empirical energy model to detect and highlight the possible Li diffusion pathway, the actual migration barriers for Li are calculated with ab initio methods. For both pathways, Li needs to migrate through the faces of adjacent oxygen tetrahedra. In the hexagonal structure in Fig. 3a, the nearest neighbor stable sites (S) are separated by a single activated Li site (labeled A in Fig. 3a). In the monoclinic structure, each stable Li trigonal-bipyramidal site consists of two tetragonal sites (S1 and S2), as shown in Fig. 3b. There are two symmetrically distinct activated sites between Li bipyramids (A1 and A2). In both structures, the low-energy migration path is one-dimensional. The ab initio calculated diffusion barriers are significantly lower for the monoclinic structure than for the hexagonal

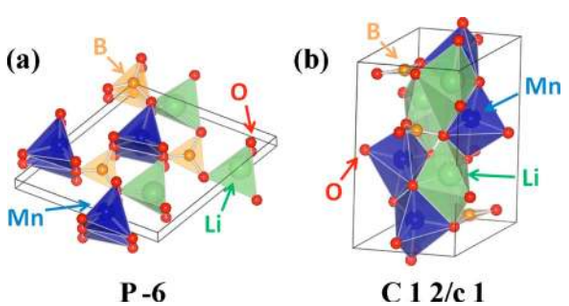

Figure 1. (Color online) Schematic diagrams of the (a) hexagonal and (b) monoclinic $LiMnBO_3$ structure.

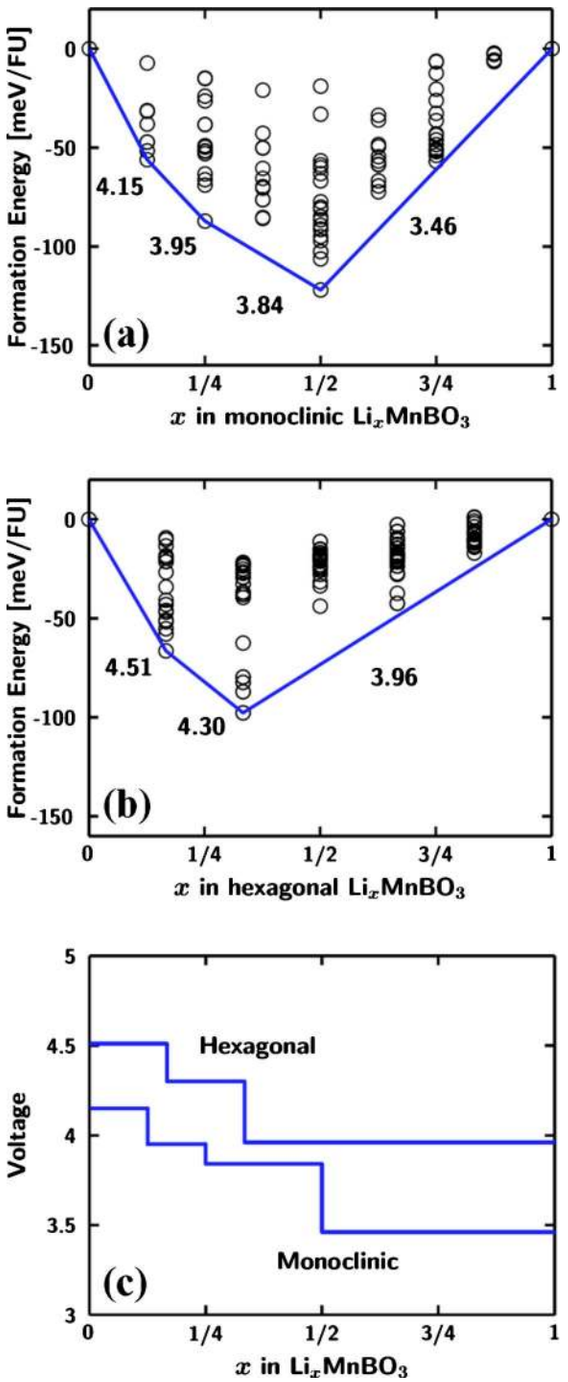

Figure 2. (Color online) Calculated formation energies for intermediate states of lithiation for the (a) monoclinic and (b) hexagonal $LiMnBO_3$, and (c) the corresponding voltage profiles of both the monoclinic and hexagonal $LiMnBO_3$.

structure. In the hexagonal form, the migration barrier is 529 meV for the delithiated structure and 723 meV for the lithiated structure. In the monoclinic structure, the barriers are significantly lower with migration energies of 395 meV in the delithiated state and 509 meV in the lithiated state.

Figure 4 shows the XRD patterns of $LiMnBO_3$ synthesized by a conventional solid state method. A homogeneous monoclinic $LiMnBO_3$ was formed when fired at 500°C, and the hexagonal

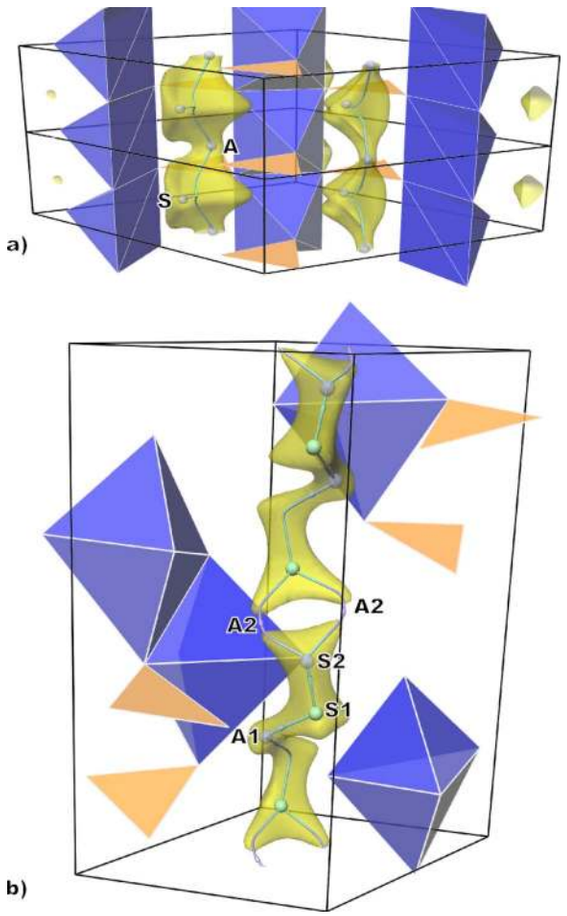

Figure 3. (Color online) Schematic diagrams of the calculated diffusion pathways for the (a) hexagonal and (b) monoclinic $LiMnBO_3$. Blue polyhedra contain Mn, yellow triangles are BO_3 groups, and the yellow contours are an isoenergy surface for Li representing the possible diffusion pathway.

phase was obtained when fired at 800°C. Both the monoclinic and hexagonal phases coexisted if fired at 600°C. Our finding that the monoclinic phase is the low temperature phase and the hexagonal

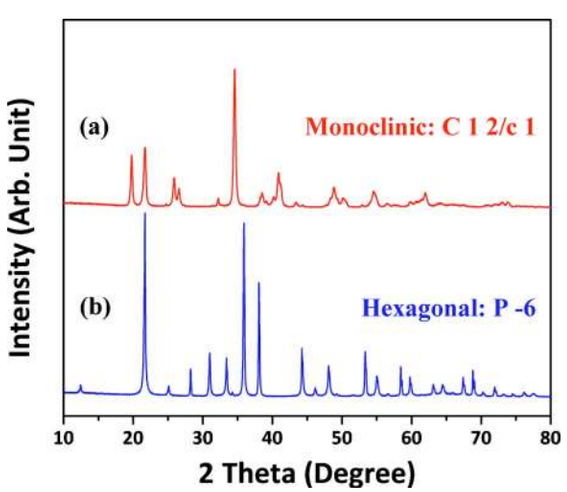

Figure 4. (Color online) XRD patterns of $LiMnBO_3$ samples fired at (a) 500°C and (b) 800°C for 10 h in an argon atmosphere.

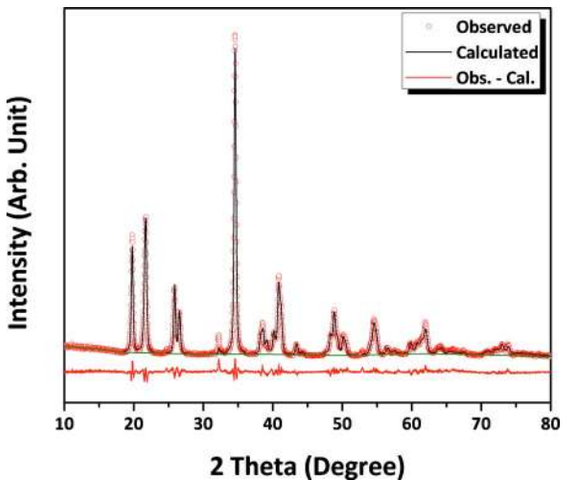

Figure 5. (Color online) Profile matching of the XRD pattern of the monoclinic $LiMnBO_3$.

phase is the high temperature phase in the $LiMnBO_3$ system agrees with the previous work.[3,14,16] The Rietveld refinement on the monoclinic $LiMnBO_3$ phase is shown and summarized in Fig. 5 and Table II. Table III summarizes the site occupancies in monoclinic $LiMnBO_3$. The structural parameters are in good agreement with values previously reported.[16]

Figures 6a and 6b show SEM images of the hexagonal and monoclinic $LiMnBO_3$ after firing. The particle size of hexagonal $LiMnBO_3$ in Fig. 6a reaches up to 700 nm, which could be a result of the high temperature firing. The monoclinic phase in Fig. 6b has 100 nm average particle size, but a rather wide size distribution is observed with a particle size ranging from approximately 80 to 250 nm. When monoclinic $LiMnBO_3$ was mixed with carbon by planetary ballmilling, the average particle size remained about 100 nm but with a narrower size distribution, as shown in Fig. 6c. The particle size of C-coated $LiMnBO_3$ (Fig. 6d) is also about 100 nm with a narrow size distribution.

The charge and discharge (second) cycle curves for the $LiMnBO_3$ compounds are shown in Fig. 7. For hexagonal $LiMnBO_3$ in Fig. 7a, the discharge capacity is less than 10 mAh/g at a C/20 rate within 4.5–2.0 V. For the monoclinic $LiMnBO_3$ without any optimization, the second discharge capacity is 34 mAh/g at a C/20 rate within the same voltage window in Fig. 7b. It is generally known that percolation between an active material and carbon in an electrode affects the degree of polarization.[29] Therefore, in order to reduce polarization, $LiMnBO_3$ and carbon black were mixed by planetary ballmilling instead of manual mixing. Figure 7c shows the voltage curve of the planetary ballmilled monoclinic $LiMnBO_3$ in the second cycle. The capacity is clearly improved, and a second cycle discharge capacity of 65 mAh/g is achieved at a C/20 rate. We tried to coat a conductive carbon phase on $LiMnBO_3$ particles, as it is a well-known approach to enhance electron conduction throughout an electrode.[30,31] For $LiFeBO_3$, C-coating has been shown to be effective to reduce polarization and, thus, increase capacities.[32-34] Carbon-coated samples were obtained by adding 10 wt % sucrose into $LiMnBO_3$, mixing by planetary ballmilling for 12 h, and then annealing at 500°C for 5 h in an argon atmosphere. Combustion infrared detection analysis revealed that 3.84 wt % of carbon remained after annealing. Figure 8 is the high resolution TEM image of the sucrose-added and annealed monoclinic $LiMnBO_3$, indicating that the carbon phase forms a coating layer on the surface with a thickness of about 2.5 nm. An electrode mix of this sample was prepared by planetary ballmilling the ingredients. Figure 7d shows the voltage curve of the C-coated monoclinic $LiMnBO_3$ as a function of a specific capacity in the second cycle. As seen in the figure, the C-coating improves the discharge capacity to 100 mAh/g at a C/20 rate within 4.5–2.0 V. The 10 cycles of the charge and discharge capacity of the C-coated monoclinic $LiMnBO_3$ cathode are shown in Fig. 9, which was done by constant current and constant voltage (CCCV) mode. The capacity decreased by approximately 3.4% per cycle.

Figure 10 shows the XRD patterns of the C-coated monoclinic $LiMnBO_3$ before and after cycling. In order to obtain the charged state XRD patterns, $LiMnBO_3$ was charged galvanostatically with a C/20 rate, after which a constant voltage charging at 4.5 V was imposed for 10 h (CCCV mode). For the XRD pattern of the discharged state, the same CCCV mode was applied at 2.0 V. The charge and discharge capacities were about 100 mAh/g. Comparison of the charged state XRD patterns in Figs. 10a and 10c to the discharged state patterns in Figs. 10b and 10d indicates that no new phases formed during the charge and discharge, providing some evidence that $LiMnBO_3$ functions by topotactic lithiation/delithiation. The patterns indicate a reversible intercalation reaction because the major peaks shift slightly upon charging, as shown in Figs. 10a and 10c, and shift back to the original position during discharging, as shown in Figs. 10b and 10d.

Discussion.— While the $LiMnBO_3$ polymorphs may appear drastically different, they share many commonalities: the Mn coordination is five and all Li is approximately tetrahedrally coordinated (if considering only the top or bottom half of the trigonal–bipyramids in the monoclinic structure). Both structures consist of columns of edge-sharing Mn polyhedra linked by planar borate groups and lithium polyhedra. Considering this, it is not surprising that they differ by only 5 meV/at. in energy. At the same time, the polymorphs differ in a few substantial ways. Mn is a square pyramidal coordinated in the hexagonal structure and trigonal–bipyramidal in the monoclinic form. The network connectivity between the polyhedral sites is also different in the two polymorphs. In the hexagonal form, three neighboring Mn columns are joined by either a stacked series of borate groups or a stacked series of Li

Table II. Rietveld refinement result of monoclinic $LiMnBO_3$.

Space Group	Ratio (%)	a (Å)	b (Å)	c (Å)	V (Å^3)	GOF	R_p	R_{exp}
C12/c1	99.7	5.1928	8.9641	10.3741	482.6791	3.70	7.81	5.65
P-6	0.3	8.2463	8.2463	3.1363	184.7003			

Table III. Site occupancy of monoclinic $LiMnBO_3$.

	Li		Mn		B	O		
Site	Li1	Li2	Mn1	Mn2	B	O1	O2	O3
Occupancy	0.6567	0.5	0.4784	0.4986	0.9934	0.8990	0.9824	1
ICSD	0.5	0.5	0.5	0.5	1	1	1	1

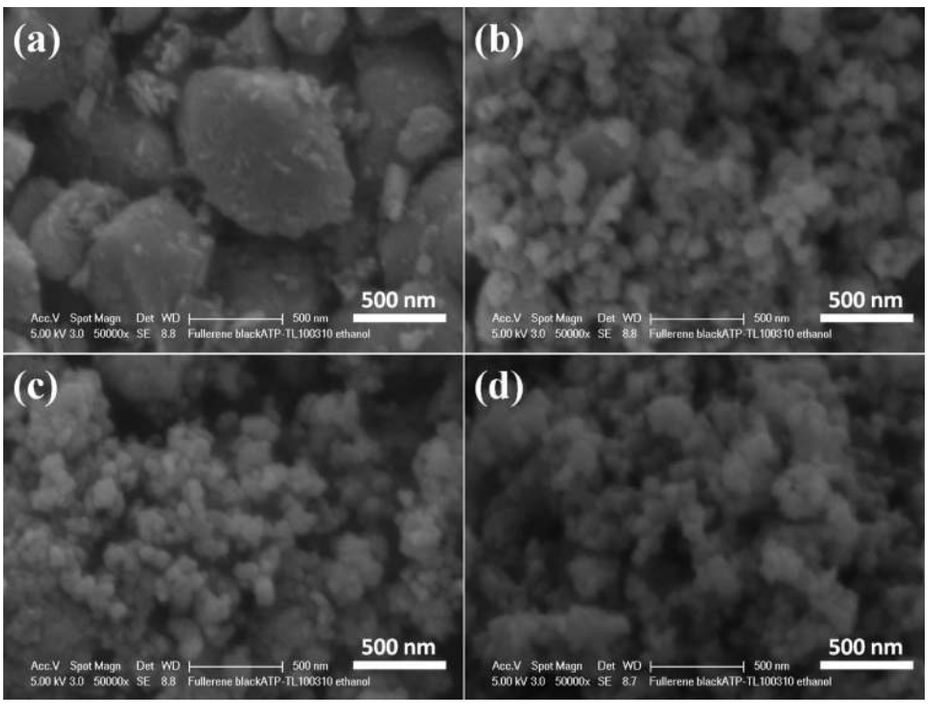

Figure 6. SEM images of the differently prepared $LiMnBO_3$ samples: (a) the hexagonal $LiMnBO_3$ fired at 800°C, (b) the monoclinic $LiMnBO_3$ fired at 500°C, (c) planetary ballmilled monoclinic, and (d) C-coated and planetary ballmilled $LiMnBO_3$ samples.

groups, as shown in Fig. 1a. In the monoclinic structure, three adjacent Mn columns are always joined by a repeating pattern of two borate groups followed by two lithium groups. Finally, there is a substantial difference in the energy of the delithiated $MnBO_3$ state of each polymorph. The monoclinic $MnBO_3$ is preferred over the hexagonal phase by 76 meV/at. The difference in average voltage, 4.11 and 3.70 V for the hexagonal and monoclinic cathodes, respectively, is almost entirely due to the difference in stability of the delithiated phases. While monoclinic $MnBO_3$ is thermodynamically unstable by 140 meV/at., as summarized in Table I, the delithiated hexagonal phase has a considerably higher driving force to decompose.

This difference in the stability of the delithiated states may influence the battery performance. Because the monoclinic $MnBO_3$ phase is energetically preferred, monoclinic $LiMnBO_3$ may be less susceptible to decomposition upon Li extraction. This is one possible explanation for the different electrochemical behaviors between $LiMnBO_3$ polymorphs.

The calculated activation barriers suggest that differences in Li diffusion may also explain the difference in the electrochemical performance between the monoclinic and hexagonal phases. While slightly higher than the calculated relevant diffusion barriers in current cathode materials such as $LiCoO_2$, $LiFePO_4$, and $LiMn_2O_4$,[35-37] the monoclinic barrier energies (395 and 509 meV) are sufficiently low to produce reasonable diffusion constants as shown in the analysis done by Kang et al.[38] The barriers are comparable to those in other potential electrode materials such as I–Li_2NiO_2 and $Li_2Ti_2O_4$

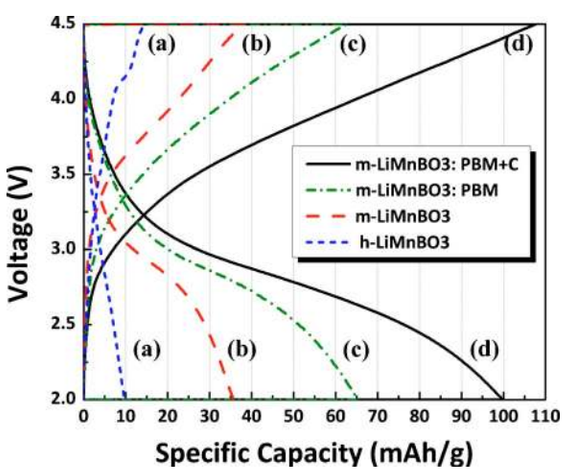

Figure 7. (Color online) Second charge and discharge capacities of differently prepared $LiMnBO_3$ samples at a C/20 rate: (a) the hexagonal phase without optimization, (b) the monoclinic phase without optimization, (c) the monoclinic phase with planetary ballmilling (PBM), and (d) the monoclinic phase with planetary ballmilling and C-coating (PBM + C).

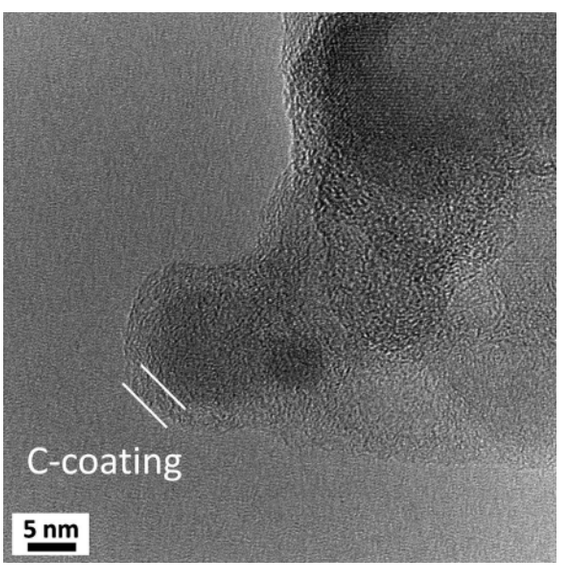

Figure 8. HRTEM image of the C-coated monoclinic $LiMnBO_3$.

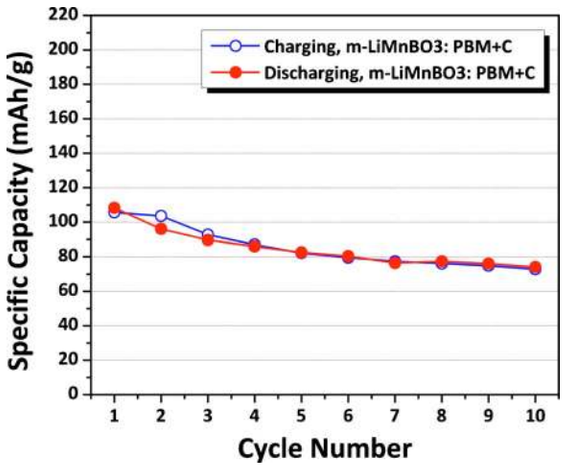

Figure 9. (Color online) Charge and discharge capacities obtained in CCCV mode as a function of a cycle number.

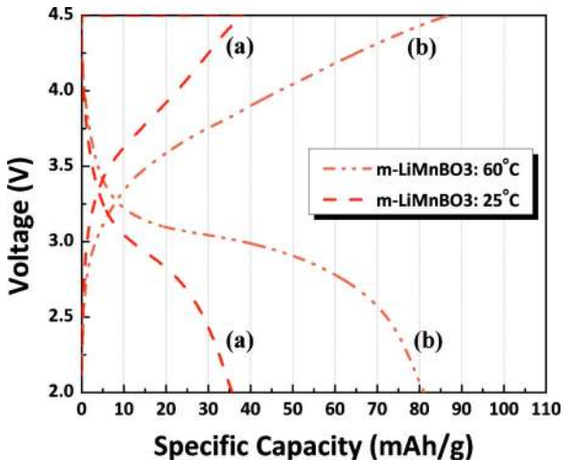

Figure 11. (Color online) Voltage curves of $LiMnBO_3$ samples without C-coating as a function of specific capacity tested at (a) 25°C and (b) 60°C at a C/20 rate.

spinel.[38,39] In contrast, the hexagonal phase's lithiated barrier energy of 723 meV is large enough to exclude the bulk of the material from a significant electrochemical performance.

In addition, considering that both the hexagonal and monoclinic phases suffer from large polarization, it is possible that their charging is incomplete at the 4.5 V cutoff. The hexagonal $LiMnBO_3$, whose calculated average voltage is 4.11 V (compared to 3.7 V for hexagonal $LiMnBO_3$), would be more limited in charging by such polarization. A significant factor in the capacity difference between the two polymorphs is surely the larger particle size of the hexagonal $LiMnBO_3$, as shown in Figs. 6a and 6b. The larger particle size is likely due to the higher temperature required to obtain the hexagonal $LiMnBO_3$ phase over the monoclinic phase. While the synthesis condition for hexagonal $LiMnBO_3$ in this work is similar to that in previous papers,[3,14] it should not be excluded that the hexagonal $LiMnBO_3$ with a smaller particle size, prepared through a different route, would have a much better performance.

The electrochemical performance of the monoclinic $LiMnBO_3$ was noticeably improved by planetary ballmilling and by C-coating, as shown in Fig. 7. Because $LiMnBO_3$ is likely a poor electronic conductor, the homogeneous network between the $LiMnBO_3$ and carbon black in the electrode is likely to facilitate electron transport. In addition, it appears that the C-coating on the particle surface was effective in reducing polarization and increasing capacity.

Even though the capacity we achieve for $LiMnBO_3$ is still below what is needed for practical lithium ion battery cathodes, the value of 100 mAh/g shows a very substantial improvement compared to the previous reports on the hexagonal $LiMnBO_3$.[3,14] Moreover, considering the C-coating is not perfectly optimized yet, further improvement can be achieved. It should be noted that in $LiFeBO_3$ minimizing surface oxidation due to air exposure led to somewhat better results, and this could be attempted to improve the electrochemical performance of the monoclinic $LiMnBO_3$.[40,41]

Our results at different temperatures suggest that the monoclinic $LiMnBO_3$ may also have an intrinsic kinetic limitation. Figure 11 shows the voltage curves of the monoclinic $LiMnBO_3$ without C-coating at different testing temperatures. It is clear that more lithium can be extracted from and inserted into the cathode at 60°C than at 25°C. Also, the cell at 60°C shows a much less polarization than that at 25°C. Enhanced kinetics at a higher temperature may be related to Li diffusion, which is a thermally activated process, and indicate that the material still has room to improve the electrochemical performance. If the material is intrinsically transport limited (electron or Li^+), further improvement of its electrochemical properties could be achieved by reducing the diffusion length. Finally, it should be noted that Li^+ transport in the monoclinic $LiMnBO_3$ is one-dimensional through the chains of connected Li-bipyramids. As in $LiFePO_4$, such 1D diffusion can be degraded very significantly by the presence of channel blocking defects.[42] Hence, focus on better characterizing the structure and its site occupancy may contribute to a better understanding of this material and its electrode performance.

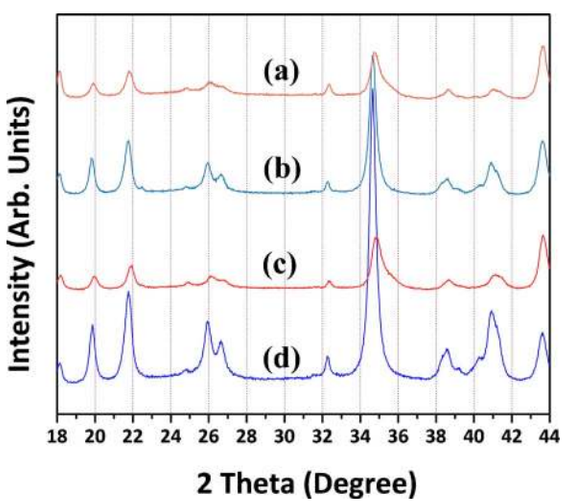

Figure 10. (Color online) XRD of cycled electrode materials: (a) after tenth charge, (b) after first discharge, (c) after first charge, and (d) before cycling. To obtain charged and discharged state, the electrodes were charged and discharged in CCCV mode within 4.5–2.0 V with C/20 rate.

Conclusions

We calculated the structural stability and electrochemical properties of $LiMnBO_3$ compounds by an ab initio computational study and report for the first time the electrochemical properties of the monoclinic $LiMnBO_3$ phase. A second discharge capacity of 100 mAh/g was achieved for a C-coated monoclinic $LiMnBO_3$ cathode with good capacity retention over multiple cycles. This performance is considerably better than what has been achieved for $LiMnBO_3$ in the hexagonal structure.

Acknowledgments

This work was supported partly by the U.S. Department of Energy under contract no. DE-AC02-05CH11231, under the Batteries

for Advanced Transportation Technologies (BATT) program by the National Science Foundation through TeraGrid resources provided by Texas Advanced Computing Center (TACC) under grant number TG-DMR970008S, and by Robert Bosch Corporation and Umicore Specialty Oxides and Chemicals.

Massachusetts Institute of Technology assisted in meeting the publication costs of this article.

References

1. C. Masquelier, A. K. Padhi, K. S. Nanjundaswamy, and J. B. Goodenough, *J. Solid State Chem.*, **135**, 228 (1998).
2. A. Nyten, A. Abouimrane, M. Armand, T. Gustafsson, and J. O. Thomas, *Electrochem. Commun.*, **7**, 156 (2005).
3. V. Legagneur, Y. An, A. Mosbah, R. Portal, A. L. La Salle, A. Verbaere, D. Guyomard, and Y. Piffard, *Solid State Ionics*, **139**, 37 (2001).
4. A. K. Padhi, K. S. Nanjundaswamy, and J. B. Goodenough, *J. Electrochem. Soc.*, **144**, 1188 (1997).
5. S. Y. Chung, J. T. Bloking, and Y. M. Chiang, *Nature Mater.*, **1**, 123 (2002).
6. B. Kang and G. Ceder, *Nature (London)*, **458**, 190 (2009).
7. A. Yamada, S. C. Chung, and K. Hinokuma, *J. Electrochem. Soc.*, **148**, A224 (2001).
8. Y. S. Meng and M. E. Arroyo-de Dompablo, *Energy Environ. Sci.*, **2**, 589 (2009).
9. M. K. Aydinol, A. F. Kohan, G. Ceder, K. Cho, and J. Joannopoulos, *Phys. Rev. B*, **56**, 1354 (1997).
10. F. Zhou, M. Cococcioni, K. Kang, and G. Ceder, *Electrochem. Commun.*, **6**, 1144 (2004).
11. L. Wang, T. Maxisch, and G. Ceder, *Chem. Mater.*, **19**, 543 (2007).
12. S. P. Ong, L. Wang, B. Kang, and G. Ceder, *Chem. Mater.*, **20**, 1798 (2008).
13. S. P. Ong, A. Jain, G. Hautier, B. Kang, and G. Ceder, *Electrochem. Commun.*, **12**, 427 (2010).
14. J. L. Allen, K. Xu, S. S. Zhang, and T. R. Jow, *Mater. Res. Soc. Symp. Proc.*, **730**, 9 (2002).
15. L. Chen, Y. M. Zhao, X. N. An, J. M. Liu, Y. Z. Dong, Y. H. Chen, and Q. Kuang, *J. Alloys Compd.*, **494**, 415 (2010).
16. O. S. Bondareva, M. A. Simonov, Y. K. Egorovtismenko, and N. V. Belov, *Sov. Phys. Crystallogr.*, **23**, 269 (1978).
17. R. K. Li, C. T. Chen, and C. Greaves, *Phys. Rev. B*, **66**, 052405 (2002).
18. J. P. Perdew, K. Burke, and M. Ernzerhof, *Phys. Rev. Lett.*, **77**, 3865 (1996).
19. S. L. Dudarev, G. A. Botton, S. Y. Savrasov, C. J. Humphreys, and A. P. Sutton, *Phys. Rev. B*, **57**, 1505 (1998).
20. F. Zhou, C. A. Marianetti, M. Cococcioni, D. Morgan, and G. Ceder, *Phys. Rev. B*, **69**, 201101(R) (2004).
21. F. Zhou, T. Maxisch, and G. Ceder, *Phys. Rev. Lett.*, **97**, 155704 (2006).
22. L. Wang, T. Maxisch, and G. Ceder, *Phys. Rev. B*, **73**, 195107 (2006).
23. G. Kresse and J. Furthmuller, *Phys. Rev. B*, **54**, 11169 (1996).
24. G. Kresse and D. Joubert, *Phys. Rev. B*, **59**, 1758 (1999).
25. G. Bergerhoff, R. Hundt, R. Sievers, and I. D. Brown, *J. Chem. Inf. Comput. Sci.*, **23**, 66 (1983).
26. G. L. W. Hart and R. W. Forcade, *Phys. Rev. B*, **77**, 224115 (2008).
27. A. Y. Toukmaji and J. A. Board, *Comput. Phys. Commun.*, **95**, 73 (1996).
28. G. Mills, H. Jonsson, and G. K. Schenter, *Surf. Sci.*, **324**, 305 (1995).
29. M. Gaberscek, M. Kuzma, and J. Jamnik, *Phys. Chem. Chem. Phys.*, **9**, 1815 (2007).
30. Z. H. Chen and J. R. Dahn, *J. Electrochem. Soc.*, **149**, A1184 (2002).
31. H. Huang, S. C. Yin, and L. F. Nazar, *Electrochem. Solid-State Lett.*, **4**, A170 (2001).
32. Y. Z. Dong, Y. M. Zhao, Z. D. Shi, X. N. An, P. Fu, and L. Chen, *Electrochim. Acta*, **53**, 2339 (2008).
33. A. Abouimrane, M. Armand, and N. Ravet, *Electrochem. Soc. Proc.*, **2003–2020**, 15 (2003).
34. A. Yamada, N. Iwane, Y. Harada, S.-i. Nishimura, Y. Koyama, and I. Tanaka, *Adv. Mater. (Weinheim, Ger.)*, **22**, 3583 (2010).
35. A. Van der Ven and G. Ceder, *J. Power Sources*, **97–98**, 529 (2001).
36. D. Morgan, A. Van der Ven, and G. Ceder, *Electrochem. Solid-State Lett.*, **7**, A30 (2004).
37. B. Xu and S. Meng, *J. Power Sources*, **195**, 4971 (2010).
38. K. Kang, D. Morgan, and G. Ceder, *Phys. Rev. B*, **79**, 014305 (2009).
39. J. Bhattacharya and A. Van der Ven, *Phys. Rev. B*, **81**, 104304 (2010).
40. J. F. Martin, A. Yamada, G. Kobayashi, S. I. Nishimura, R. Kanno, D. Guyomard, and N. Dupre, *Electrochem. Solid-State Lett.*, **11**, A12 (2008).
41. M. Cuisinier, J. F. Martin, N. Dupre, A. Yamada, R. Kanno, and D. Guyomard, *Electrochem. Commun.*, **12**, 238 (2010).
42. R. Malik, D. Burch, M. Bazant, and G. Ceder, *Nano Lett.*, **10**, 4123 (2010).